ORCA – Online Research @ Cardiff

Manga, Michael, Fauria, Kristen E., Lin, Christina, Mitchell, Samuel J., Jones, Meghan, Conway, Chris E., Degruyter, Wim , Hosseini, Behnaz, Carey, Rebecca, Cahalan, Ryan, Houghton, Bruce F., White, James D.L., Jutzeler, Martin, Soule, S. Adam and Tani, Kenichiro 2018. The pumice raft-forming 2012 Havre submarine eruption was effusive. Earth and Planetary Science Letters 489 , pp. 49-58. 10.1016/j.epsl.2018.02.025

Publishers page: http://dx.doi.org/10.1016/j.epsl.2018.02.025

The pumice raft-forming 2012 Havre submarine eruption was effusive

Michael Manga[1*], Kristen E. Fauria[1,3], Christina Lin[1], Samuel J. Mitchell[2], Meghan Jones[3], Chris Conway[4], Wim Degruyter[5], Behnaz Hosseini[1], Rebecca Carey[6], Ryan Cahalan[7], Bruce F. Houghton[2], James D.L. White[8], Martin Jutzeler[6], S. Adam Soule[3], Kenichiro Tani[4]

1 Department of Earth and Planetary Science, University of California, Berkeley, CA 94720, USA

2 Department of Geology and Geophysics, University of Hawai'i at Mānoa, 1680 East West Road, Honolulu, HI 96822, USA

3 Woods Hole Oceanographic Institution, Woods Hole, MA 02543, USA

4 National Museum of Nature and Science, 4-1-1 Amakubo, Tsukuba, Ibaraki 305-0005, Japan

5 School of Earth and Ocean Sciences, Cardiff University, Main Building, Park Place, Cardiff, CF10 3AT, Wales, UK

6 School of Physical Sciences and Centre of Excellence in Ore Deposits (CODES), University of Tasmania, Hobart, TAS 7001, Australia

7 School of Earth and Atmospheric Sciences, Georgia Institute of Technology, 311 Ferst Drive, Atlanta, GA 30332, USA

8 Department of Geology, University of Otago, PO Box 56, Dunedin 9054, New Zealand

*Corresponding author, manga@seismo.berkeley.edu

January 17, 2018, revised February 13, 2018

Abstract

A long-standing conceptual model for deep submarine eruptions is that high hydrostatic pressure hinders degassing and acceleration, and suppresses magma fragmentation. The 2012 submarine rhyolite eruption of Havre volcano in the Kermadec arc provided constraints on critical parameters to quantitatively test these concepts. This eruption produced a > 1 km^3 raft of floating pumice and a 0.1 km^3 field of giant (>1 m) pumice clasts distributed down-current from the vent. We address the mechanism of creating these clasts using a model for magma ascent in a conduit. We use water ingestion experiments to address why some clasts float and others sink. We show that at the eruption depth of 900 m, the melt retained enough dissolved water, and hence had a low enough viscosity, that strain-rates were too low to cause brittle fragmentation in the conduit, despite mass discharge rates similar to Plinian eruptions on land. There was still, however, enough exsolved vapor at the vent depth to make the magma buoyant relative to seawater. Buoyant magma was thus extruded into the ocean where it rose, quenched, and fragmented to produce clasts up to several meters in diameter. We show that these large clasts would have floated to the sea surface within minutes, where air could enter pore space, and the fate of clasts is then controlled by the ability to trap gas within their pore space. We show that clasts from the raft retain enough gas to remain afloat whereas fragments from giant pumice collected from the seafloor ingest more water and sink. The pumice raft and the giant pumice seafloor deposit were thus produced during a clast-generating effusive submarine eruption, where fragmentation occurred above the vent, and the subsequent fate of clasts was controlled by their ability to ingest water.

Keywords: submarine eruption; pumice; fragmentation; raft; conduit flow; X-ray tomography

Highlights:

Havre magma entered the ocean before fragmenting.

Clasts were produced by quenching buoyant magma in the ocean.

Buoyant > 1 m diameter pumice blocks floated to the ocean surface.

Clasts with enough isolated porosity and trapped gas floated in a raft while the rest sank.

1. Introduction

Submarine volcanic eruptions may be fundamentally different from those on land owing to the high hydrostatic pressure provided by the ocean which inhibits degassing and hence magma acceleration and fragmentation. Our understanding and record of such eruptions are limited by the challenge in directly witnessing eruption processes and sampling and characterizing the deposits from those eruptions. Indeed, overcoming this biased understanding of volcanic eruptions was highlighted by the 2017 National Academies report (National Academies, 2017): "What processes govern the occurrence and dynamics of submarine explosive eruptions"?

Silicic magmas that erupt more than a few hundred meters below sea-level give rise to eruption styles distinct from those on land owing to the contrasting properties of the ambient fluid (water vs air) into which the magmas erupt (Cashman and Fiske, 1991). For example, clasts that erupt at the seafloor are initially buoyant, but ingest water into pore space as they cool (e.g., Whitham and Sparks, 1986); hence fragmented magma can either rise to the surface to form rafts, or feed submarine density currents if the clasts become waterlogged (Allen and McPhie, 2009).

One distinctive facies of both modern and ancient clastic deposits from submarine silicic eruptions is voluminous deposits of giant (>1 m) pumice clasts (e.g., Kato, 1987; Kano et al., 1996; Kano, 2003; Allen and McPhie, 2009; Allen et al., 2010; Jutzeler et al., 2014). These clasts often have one or more quenched margins with curviplanar joints perpendicular to the cooling surface that suggest they quenched in water (e.g., Wilson and Walker, 1985; Allen et al., 2010; Von Lichtan et al., 2016; Figure 1). Otherwise, submarine pumice vesicularities are similar to those produced in subaerial Plinian eruptions (e.g., Barker et al., 2012) and hence it has been proposed that fragmentation mechanisms are also similar for large (> 1 km^3) submarine equivalents (e.g., Allen and McPhie, 2009; Shea et al., 2013). There are, however, textural differences: pumice clasts from deep submarine eruptions tend to have smaller bubble number densities, lack very small vesicles (<10 μm), and display a narrower range of modal vesicle sizes (Rotella et al., 2015). Clasts have also been proposed to form from buoyant bubbly magma as it exits the vent by “viscous detachment or by the development of cooling joints” (Rotella et al., 2013), an eruption style that would not fit neatly into either the “effusive” or “explosive” categories used to describe subaerial eruptions. Pumice clasts can also form by spallation from a pumiceous carapace on effusive domes (e.g., Cas and Wright, 1987; Kano, 2003; Allen et al., 2010).

In July 2012, approximately 1.2 km^3 of rhyolite pumice clasts erupted at a water depth of 900 m from the submarine Havre volcano in the Kermadec volcanic arc (Carey et al., 2014; Figure 1). The majority of the pumiceous material formed a raft of floating clasts that was widely dispersed in the western Pacific Ocean (Jutzeler et al., 2014; Carey et al., 2018). A second clastic product of this eruption is a 0.1 km^3 deposit of giant pumice clasts on the seafloor around the inferred vent. An outstanding question is whether these seafloor giant pumice clasts and raft pumice originated from the same eruptive phase. Though not conclusive, the vesicularities, composition, microtextures (e.g., bubble number densities, crystallinity, microlite mineralogy), and macrotextures (e.g., banding), are similar as is their primary axis of dispersal (Carey et al., 2018). If the raft and seafloor pumice did originate from the same eruptive episode, their different fate, i.e., whether they floated or sank, thus requires seafloor giant pumice to ingest water more effectively than clasts that were transported into the raft.

Here we use a model for magma ascent, constrained by estimates of the eruption rate for the pumice raft and a variety of measurements on erupted materials, to show that buoyant magma reached the seafloor prior to fragmenting. We then investigate how pumice clasts from the raft and seafloor ingest water as they cool and find that seafloor pumice ingest water more efficiently by trapping very little gas. We thus infer that vesicular coherent magma extruded into the ocean. The magma quenched and fragmented non-explosively to form the pumice clasts that then either remained afloat because they retained enough gas or, if they waterlogged, settled to the seafloor.

2. Methods

2.1 Conduit model

Magma ascent is simulated using a one-dimensional two-phase model for steady flow, modified from Degruyter et al. (2012) and Kozono and Koyaguchi (2009). Pressure at the vent is 9 MPa corresponding to a water depth of 900 m. The conduit length is 8.1 km with a pressure at its base of 200 MPa. Crystallinity is 5% (Carey et al., 2018) and crystals do not grow or nucleate during ascent. The effects of crystals and bubbles on viscosity are based on the models of Costa (2005) and Llewellin and Manga (2005), respectively (supplement S1). Water content in the melt is 5.8 weight % based on 16 plagioclase-hosted melt inclusions from a seafloor giant pumice clast (supplement S2). Number density of bubbles is 10^{14} m^{-3} (Rotella et al., 2015), high enough that we can assume equilibrium bubble growth (Gonnermann and Manga, 2005); we obtain similar ascent rates for number densities 100 times lower and higher. The effects of temperature and dissolved water on viscosity are computed using Giordano et al. (2008) and the measured composition (supplement S3) and water content. Temperature is set to 850 ± 20 °C based on cpx-opx Fe-Mg exchange (Putirka, 2008) in ten measured cpx and opx compositions. Magma can fragment in the conduit if the strain-rate $\dot{\gamma}$ exceeds a critical value (e.g., Papale, 1999)

$$\dot{\gamma} > 10^{-2} G/\mu \,, \qquad (1)$$

where $G = 10^{10}$ Pa is the shear modulus (e.g., Simmons, 1998) and μ is the melt viscosity. We compute both the strain-rate at the conduit walls and the elongation strain-rate in the center of the conduit.

It is important to recognize that in addition to uncertainties in magma properties there are also model assumptions that affect strain-rates, ascent velocity, and vesicularity at the vent. For example, the ascending magma is assumed to be isothermal and Newtonian, we neglect viscous heating and shear localization in the magma, and we do not permit non-equilibrium bubble growth. We also use a geometrically idealized conduit shape. In addition, we assume that at any given depth the bubble size is uniform and use this bubble size to compute a permeability. There are, however, bubbles much larger than the mean size which, owing to the nonlinearity of permeability-bubble size relationships, could lead to higher permeability and more outgassing.

2.2 Floatation experiments

To determine the propensity for Havre pumice clasts to remain afloat after reaching the raft at the ocean surface, we conducted 11 experiments in which we measured the amount of liquid water and trapped gas within cm-sized clasts from the Havre raft (7 samples) and fragments of seafloor giant pumice (4 samples). We heated dry raft clasts and giant pumice fragments to a range of temperatures up to 700°C and placed them on the water surface for ten minutes. We then rapidly encased the clasts in wax – to minimize further changes in the distribution of internal fluids – and imaged the clasts at 1.22 μm resolution using X-ray computed microtomography (XRT) with 30 keV monochromatic X-rays. To enhance the absorption contrast between the water and glass, we used a 13 weight% potassium iodide solution. Additional imaging details are provided in supplement S4. From the XRT images, we identified the volumetric content of glass, liquid water, and trapped gas within the clasts using machine learning algorithms to segment these three phases (Fauria et al., 2017).

To further quantify pumice floatation dynamics, we measured the floatation time of room temperature raft and seafloor clasts. To measure floatation times, we placed dry and ambient temperature clasts in water and noted the time at which they sank. Before the experiments, we cleaned the clasts in an ultrasonicator for ~10 min and then dried them. Once the experiments were initiated, we monitored the clasts with a camera and noted the time at which the clasts sank to the nearest minute. If clasts continued to float after the first six months of the experiments, we stopped monitoring with a camera and began checking on the clasts approximately daily and then weekly once the experiments progressed past the first year.

We measured clast weight before and after the experiments. For a subset of the clasts, primarily the seafloor clasts, we measured clast volume using photogrammetry. Specifically, we took 100-180 photographs per clast using a Canon DSLR camera with an extension tube. We processed the images and constructed volume models (Poisson surface reconstructions) using VisualSFM and MeshLab softwares. In cases where the clasts were too small to accurately measure volume using photogrammetry, we estimate pumice volume using pumice mass assuming a clast porosity of 83% (Carey et al., 2018).

2.3 Isolated porosity

Differences in isolated porosity between the raft and seafloor samples are unresolvable in the XRT scans. We thus use helium pycnometry to quantify the connected and unconnected pore space. Samples were cored, washed, dried, and weighed. The volume of the cylindrical cores was calculated based on the mean of 10 measurements of the sample diameter and height. The volume of the solid phase and isolated porosity was measured using a He-pycnometer at the University of Oregon using methods described in Giachetti et al. (2010). The pycnometry measurements and bulk volume were used to calculate the connected porosity. One seafloor sample and one raft sample were crushed, weighed, and analyzed using He-pycnometry in order to determine the solid density. The bulk vesicularity was calculated from the solid density, bulk volume, and bulk density. The isolated vesicularity was calculated from the difference between the bulk vesicularity and connected vesicularity.

3. Results

Figure 2 shows how ascent velocity, mean bubble size, melt viscosity, and vesicularity vary with depth in the conduit for conduit radii of 3, 21 and 33 m. The corresponding mass eruption rates are 4.2×10^3, 1.0×10^7 and 6.2×10^7 kg/s respectively. This model reproduces the observed vesicularity of about 80-90 % and modal vesicle size (Rotella et al., 2015; Carey et al., 2018). A conduit radius of 21 m leads to a mass eruption rate similar to the time-averaged value inferred from the volume of the pumice raft and the estimated duration of the raft-forming stage of the eruption, 9×10^6 kg/s (Carey et al., 2018). For this eruption rate, Figure 2b shows that the gas and melt remain coupled and there is negligible outgassing during ascent. The model does not account for any further modification of vesicularity of clasts after they enter the ocean.

There are uncertainties in all model parameters including, critically, those that affect viscosity: water content and temperature. However, the main conclusions are not sensitive to reasonable ranges in these parameters. For example, if we reduce the water content to 5% and temperature to 820 ^{o}C, even for an eruption rate an order of magnitude greater than inferred, 1×10^{8} kg/s, the strain-rate is still a factor of 5 too low to cause melt to fragment based on equation (1).

Figure 3 shows that reheated (> 500°C) Havre raft pumice can retain enough gas to remain buoyant. By comparison, fragments from the seafloor giant pumice are almost fully saturated (< 0.05 volume fraction gas) after they are reheated above 500°C and placed on the water surface. The results from these experiments demonstrate that hot Havre seafloor giant pumice draw in considerably more water than raft pumice. In raft pumice, some of the gas is trapped by the infiltrating water (red arrow), but there is also a significant amount of unconnected porosity (isolated bubbles). This difference is further highlighted by the pycnometry measurements. Figure 4 shows the connected and unconnected porosity analysis and reveals that seafloor giant pumice has fully connected porosity whereas raft pumice always contains isolated bubbles. These differences may be documenting samples from different parts of the conduit, or samples that experienced different vesiculation histories in the water column. A thorough analysis of textures from raft and seafloor samples may reveal not only why some clasts float, but provide further insights into ascent processes in the conduit and water column.

Figure 5 shows clast volume versus floatation time. We identify clasts that were still floating at the time of manuscript submission with red outlines. We find that floatation time increases with clast size and that raft pumice float orders of magnitude longer than seafloor pumice. We compare pumice floatation times to a diffusion model for pumice floatation from Fauria et al. (2017). The model predicts that floatation time scales as

$$\tau = \frac{4R^2}{D_a \theta^2}, \quad (2)$$

where τ is time, *2R* is clast diameter, $D_a = 1.9\times10^{-9}$ m^2/s is air-water diffusivity (Fauria et al., 2017), and θ is the fraction of pore space containing liquid water. The shaded region in Figure 5 shows predictions of equation (2) with θ between 0.1 and 0.5. Seafloor clasts match the diffusion model prediction while raft pumice float much longer than predicted and, indeed, have yet to sink. The presence of isolated bubbles (Figure 4) may explain why cold raft pumice float much longer than theoretical models predict.

4. Discussion

We now address in order three basic questions about the 2012 Havre eruption. Where and why did the magma fragment? What processes form meter-sized clasts? Why do some pumice clasts float (raft pumice) and others sink (seafloor giant pumice)?

4.1 Fragmentation

From the conduit model, strain rates never become large enough to cause brittle fragmentation within the conduit of the Havre eruption. Instead, at 86% vesicularity, the erupting magma is less dense than sea water and hence will continue to rise above the vent rather than creating a dome. What processes then create the pumice? We do not favor buoyant detachment of blebs by gravitational instabilities, one mechanism suggested for example by Rotella et al. (2013), because the separation of blebs is slow compared to the inferred extrusion velocity for the Havre eruption and we did not see fluidal-shaped clasts either near the vent or in samples from the raft. For a bleb of length l and radius *r* buoyantly rising above the extruding magma, the velocity $dl/dt \approx \frac{(\rho_w-\rho_c)gr^2}{\mu} \ln (l/r)$, where ρ_c is clast density, ρ_w is water density, and *g* is gravity (Olson and Singer, 1985). This is a Stokes flow scaling, appropriate because the magma viscosity controls extrusion prior to fragmentation. Choosing $l = 2r$ for equant bleb, $\mu = 5\times10^6$ Pa s (Figure 2), $\rho_w - \rho_c = 500$ kg m^{-3} (Rotella et al., 2015; Carey et al., 2018), and *l*=5 m, we obtain an ascent speed of 4 cm/s, much less than the velocity at the vent of 14 m/s (figure 2). The melt is so viscous that ductile processes are too slow to produce clasts.

Instead, we suggest that the surface of extruded magma will quench in the ocean, producing a network of cracks perpendicular to the magma surface. Highly vesicular magma is prone to quench fragmentation and the temperature difference between magma and seawater is sufficient to create cracks (van Otterloo et al., 2015), possibly aided by continued vesiculation. Crack propagation speeds can be tens to hundreds of meters per second (van Oterloo et al., 2015) so that a large volume of fragmented debris can be produced very quickly. Although a range of fragment sizes will be produced, they will not be able to separate and rise unless they can also float upwards fast enough from the extruding magma. Smaller fragments may weld together, or may break off larger clasts or the side of the extruding spine of magma if the spine extends above the vent.

4.2 Separating pumice from extruding magma

The terminal rise speed U of clasts produced by quenching and surrounded by water, idealized here as spherical with radius R, is

$$U = \sqrt{\frac{8(\rho_w - \rho_c)gR}{3\rho_w C_D}} \quad . \qquad (3)$$

Given the very high Reynolds number ($\sim 10^7$), the drag coefficient C_D is approximately 0.3 (e.g., Batchelor, 1967). Equation (2) also neglects entrainment by the buoyant warm water heated by the clasts, which would increase velocity. With a conduit radius of 21 m the vent velocity is 14 m/s (Figure 2), and clasts with R>4.5 m will rise faster than the extrusion speed, at least before they ingest water. Exit velocity is inversely related to conduit radius owing to mass conservation. If the vent widens by 40% at the seafloor, the minimum radius R for detachment decreases to 1.2 m. There are uncertainties in both the mass eruption rate that constrains the exit velocity and the parameters that affect the minimum size of clasts computed from equation (3), but predicted meter-sized clasts are similar to typical sizes of the giant pumice on the seafloor, averaging 1-1.6 m near the vent and increasing with dispersal distance (Carey et al., 2018).

4.3 Reaching the sea surface

Clasts that detach from the extruded magma will rise through the ocean until they saturate with water. Once saturated, clasts will become negatively buoyant and sink to the seafloor. For meter-sized clasts, water ingestion is limited not by permeability but by the ability of water vapor in the clast to cool, condense and draw in liquid (appendix A). As cooling is slower than permeable flow, the rate of heat loss from the interior of the pumice will determine the time to saturation. To compute the evolution of clast density through water ingestion, and hence their ascent through the ocean, we model the cooling, condensation, and thus flow of liquid water into spherically symmetric clasts using experimentally measured rates of heat loss, and compute the rise speed of the clasts using equation (3) from the time-evolving mean clast density (assuming fully connected porosity). We allow gas in the clasts to expand as the ambient pressure decreases (appendix B) which is significant because water vapor density is > 15 kg/m^3 at 900 m water depth and ~ 1 kg/m^3 at the surface. Additional joints within clasts would enhance water ingestion and cooling beyond what we model. We neglect any possible further vesiculation within clasts as they rise through the ocean. Although clasts may remain hot as they ascend and can continue to exsolve water, vesicles need not grow if the pore space is connected to permit gas leakage to the ocean (e.g., Kueppers et al., 2012). Figure 6 shows the time required for clasts of different vesicularities to reach the ocean surface before they become negatively buoyant in water. Meter-sized clasts, such as the seafloor giant pumice, are expected to reach the raft at the ocean surface and will have ingested little water. The initial sizes of raft pumice are not known, but Figure 6 suggests that a minimum size of about one meter is required for clasts to reach the surface.

4.4 To sink or float?

The long-term fate of floating pumice on the sea surface depends on their ability to ingest additional water as they float. The ascent model predicts that there is virtually no liquid in meter-sized and larger clasts as they reach the sea surface owing to the expansion of vapor in the clasts during ascent (appendix B). However, the seafloor deposit of giant pumice comprises clasts up to 9 m in diameter (Carey et al., 2018). Some of those may include pumices that are large enough to reach the sea surface, but are trapped underneath floating pumice and remain fully surrounded by water, in which case we would expect them to sink once the water vapor cools and condenses

(Allen et al., 2008). Others must have reached the sea surface and subsequently saturated with water.

Once pumice reaches the sea surface, we expect air to replace most of the water vapor in the pore space because gas diffusion and exchange is rapid, and is further enhanced as clasts crack or break. Air-filled pumice is known to float much longer (e.g., Whitham and Sparks, 1986; Manville et al., 1989; Dufek et al.., 2007; Jutzeler et al., 2017) than the time it takes for porous flow to allow water to infiltrate (Vella and Huppert, 2007). Instead, the ability of clasts to float is controlled by the propensity of the infiltrating water to trap gas bubbles within the pore space and/or the presence of isolated vesicles. If enough gas is trapped during infiltration of water, the clasts will float until this gas diffuses through the water and out of the clast (Fauria et al., 2017).

The difference in isolated and connected porosity can partially explain the propensity for raft pumice to float, however, additional gas trapping is required for most clasts (Figure 4). Our experiments confirm that fragments of seafloor giant pumice ingest more water and trap less gas than raft pumice, and hence more rapidly become negatively buoyant. The presence of elongate ”tube” vesicles in some seafloor pumice has further implications for why some clasts sink preferentially to others. The elongate structure, high connectivity and anisotropic permeability of such vesicles would permit rapid clast saturation and subsequent sinking to the seafloor (Wright et al., 2006). The diversity of these textures within pumice deserves more detailed microtextural analysis.

We thus propose that what separates pumice into the raft is their ability to trap gas and the presence of isolated vesicles; clasts that cannot retain enough gas sink. Those that trap gas and/or have sufficient isolated vesicles float. Presumably the difference in gas trapping results from differences in topology of the pore space such as the number of dead-end pores. We could not, however, identify any key differences in our images. We note several caveats, however. First, we are not able to do experiments on meter-sized raft or seafloor clasts owing to the lack of intact samples and our inability to measure and image the infiltration at such large scales. We thus assume that the smaller fragments we imaged are representative of the larger clasts from their respective units. Second, we do experiments on quenched samples, whereas the vesicularity and texture of the pumice may evolve during quenching and also after their initial fragmentation. Larger clasts should take longer to ingest water, explaining why seafloor pumice clast size increases with distance from the vent (Carey et al., 2018).

4.5 The effusive eruption of Havre

The raft-forming Havre eruption was not explosive in the same manner as subaerial pumice clast-forming eruptions. This submarine style of pumice-generating eruption requires an eruption depth that is not-too-deep and not-too-shallow (Figure 7). In deeper water, with the critical depth depending on the water content of the melt, the magma will not be buoyant and will form a lava flow or dome (Figure 7c). In shallower water, the melt viscosity will be higher owing to greater gas exsolution and the magma may undergo brittle fragmentation in the conduit (Figure 7a). For the Havre mass eruption rate, composition, and water content, a vent depth of 2.8 km will lead to the erupting magma being denser than seawater (1030 kg/m^3), and a vent shallower than 290 m will allow the magma to fragment in the conduit (21 m radius) assuming that the criterion given by equation (1) is accurate. It is worth noting that the Taupo eruption which also produced giant pumice fragments, and was dominated by Plinian-phreatoplinian explosions and magmatic fragmentation in the conduit, occurred in water depths that were never more than 200 m (Wilson and Walker, 1985; Houghton et al., 2003). Mass discharge rate also matters because low ascent rates enable outgassing. For example, at Havre multiple lava domes with low-to-moderate vesicularity extruded in 2012 at the same water depth as the vent that produced the giant pumice clasts. At Sumisu Dome C in the Sumisu Dome Complex, Izu Bonin Arc, Japan, silicic pumiceous dome carapaces at 1100-1300 mbsl have high vesicularity, between 60 – 85%, and did not produce a clastic deposit (Allen et al., 2010).

The 2012 eruption that produced the pumice raft partly conforms to the eruption style proposed by Rotella et al. (2013) in which bubbly magma enters the ocean and clasts detach from the extruding magma; we favor “cooling joints” and other mechanical stresses over “viscous detachment” for Havre because the effusion velocity is so high and because we lack evidence for any wholly or partly bleb-shaped clasts; ductile processes, however, may be important for creating floating clasts from less viscous magmas (e.g., Kueppers et al., 2012).. As noted by others (e.g., Cas and Giordano, 2014; Allen and McPhie, 2009; White et al. 2015), terminology such as explosive and effusive, developed for subaerial eruptions and their deposits, may not translate well to the submarine realm where high hydrostatic pressure and the cooling effects of liquid water can modulate fragmentation.

Given that submarine giant pumice deposits are common products of historical eruptions and well documented in the rock record (Reynolds et al., 1980; Kano et al., 1996; Risso et al., 2002; McPhie and Allen, 2003; Kano, 2003; Allen and McPhie, 2009; Allen et al., 2010; Jutzeler et al., 2014; Von Lichtan et al., 2016), we infer that the 2012 Havre eruption may be an example of a relatively common style of deep submarine volcanic eruption. Modern intra-oceanic arcs, such as the Kermadec, Izu, Bonin, Mariana, and South Sandwich arcs contain many deep submarine silicic volcanoes, and similar eruptions may be common.

5. Conclusions

The 2012 pumice raft-forming eruption was produced from a vent that extruded buoyant vesicular rhyolite into the sea at speeds > 10 m/s. This lava fragmented by quenching in the ocean to produce three subpopulations of clasts. Large clasts (> 1 m) rose to the sea surface without ingesting enough water to sink. Those large clasts with sufficient isolated vesicles and/or trapped gas remained afloat in the raft. Large clasts that did not retain enough gas, and those that were trapped beneath the pumice raft, sank to create the seafloor giant pumice. Smaller clasts would not have reached the surface, ingesting water quickly and settling close to the vent, or were transported by currents if small enough.

The eruption style documented at Havre may be dominant for submarine silicic eruptions, as most submarine vents are at depths greater than a few hundred meters. Giant pumice clasts are a product, and thus an indicator, of large, deep effusive eruptions. This eruption style partitions most of the mass into distal and global ocean basins, which has implications for how we interpret past events and may ultimately lead to a re-evaluation of the volumes and magnitudes of submarine eruptions in the past.

Acknowledgements: MM, KF, CL and BH are supported by NSF 1447559. SM and BH are supported by NSF 1357443. RJC was funded by the Australian Research Council (DP110102196, DE150101190). AS is supported by NSF 1357216. MJ is supported by a National Defense Science and Engineering Graduation Fellowship. XRT was enabled by the Lawrence Berkeley National Lab Advanced Light source, beamline 8.3.2, and guidance from Dula Parkinson. Additional support was provided by the Marsden fund and the 2017 Student Mentoring and Research Teams (SMART) Program, Graduate Division, University of California, Berkeley. Fumihiko Ikegami created Figure 1d. Brian Monteleone provided assistance in SIMS analysis of melt inclusions at the Northeast National Ion Microprobe Facility. Melissa Rotella provided the raft clasts using in the floatation experiments. Thomas Giachetti provided assistance with He-pycnometry. We thank Tushar Mittal, Dan Fornari, Jocelyn McPhie, Ray Cas and an anonymous reviewer for comments, and the rest of the MESH team and Roger Revelle crew for making this science possible.

Author contributions. MM and WD modeled magma ascent. KF and CL perfomed the ingestion experiments and analysis. SM measured volatiles. CC measured composition. KF and BH did the floatation experiments. MJ measured porosity. KF and MM developed the clast ascent and ingestion model. All authors contributed to sample collection, interpretation and writing.

Appendix

A. Why ingestion is not likely to be limited by permeability for large clasts

As the interior of vapor-filled pumice cools, vapor condenses and draws in liquid water. Whether heat loss or permeability limits this ingestion of liquid depends on the ability of a clast to lose heat compared to the ability of liquid to flow into the clast – the slowest process will govern liquid ingestion.

The condensation of vapor and heat loss from the clast is similar to the classic Stefan problem except that advection of heat by liquid water drawn into the clast may dominate the heat transport. An energy balance at the vapor-liquid interface balances the conductive transport across that interface with the latent heat released

$$-\kappa \frac{dT}{dx} = \rho_s \phi L u \quad (\mathrm{A.1})$$

where u is the fluid velocity, L the latent heat, ρ_s is the density of steam, ϕ is porosity, T is temperature, κ is the thermal conductivity of the liquid-saturated clast, and x is position. The temperature distribution within the liquid-saturated part of the clast that determines the left-hand side of equation (A.1) depends on u, and we use the solution for steady-state advective-diffusion problem from Bredehoeft and Papadopulos (1965)

$$\frac{T(x) - T_a}{T_s - T_a} = \frac{e^{\beta x/a} - 1}{e^{\beta} - 1} \quad (\mathrm{A.2})$$

where $\beta = ua/D$ is a dimensionless Peclet number (ratio of advection to diffusion of heat), where D is the thermal diffusivity of the liquid-saturated clast, a is the distance from the clast surface to the steam-liquid interface, and T_a and T_s are the temperatures of the ambient water and steam-liquid interface, respectively. The solution for the infiltration speed can be obtained by solving equations (A.1) and (A.2)

$$u = \frac{D}{a} \ln\left[1 + \frac{\kappa(T_s - T_a)}{\rho_s \phi L D}\right] \quad (\mathrm{A.3})$$

If permeability limits the infiltration speed of water, a lower bound on the velocity is given by Darcy's law assuming buoyancy controls infiltration

$$u > \frac{k \rho_w g}{\mu_w \phi} \qquad (\mathrm{A.4})$$

where k is permeability, and μ_w is the viscosity of water. We use > because we neglect the additional (and likely much larger) pressure gradients from gas contraction and capillary forces that would further increase u.

Whether heat loss controls infiltration (equation A.3) or permeable flow (equation A.4) depends on which is larger – the slowest velocity is rate-limiting. Permeability is not limiting if

$$k > \frac{\mu_w \phi D}{a \rho_w g} \ln\left[1 + \frac{\kappa(T_s - T_a)}{\rho_s \phi L D}\right] \quad (\mathrm{A.5})$$

Using $D = D_w\phi + D_r(1-\phi) = 2.5\times10^{-7}$ m^2/s for $\phi = 0.8$, where D_w and D_r are the diffusivities of water and glass, respectively (Bagdassarov et al., 1994), $\kappa = 2$ Wm^{-1}K^{-1}, and conditions at the ocean surface ($T_s - T_a$=100 $^{\circ}$C, ρ_s=1 kg/m^3), we find that cooling is limiting provided $k > 1.5\times10^{-13}$ m^2 for a clast with a = 1 m. Permeability of pumice is generally larger than this value, typically > 10^{-12} m^2 for vesicularities of 70-80% (e.g., Rust and Cashman, 2004; Mueller et al., 2005; Burgisser et al., 2017; Colombier et al., 2017; Gonnermann et al., 2018). Note that the value of k from equation (A.5) is an upper bound because we ignore additional pressure gradients driving water into the clast in equation (A.4) and densities and temperature difference at greater depths decrease the velocity predicted by equation (A.2). The model also neglects any interfacial instabilities that might enhance infiltration or change effective diffusivities (e.g., Randolph-Flagg et al., 2017).

B. Cooling, ingestion and ascent model

We model the density evolution and rise of hot and initially water vapor-saturated clasts. Clast density evolves due to internal gas decompression, contraction of vapor by cooling and condensation, and from liquid water infiltration. We assume that the clast vesicularity does not change due to volatile exsolution after clasts form. By coupling a model for clast density evolution to a model for clast rise speed (equation 3), we can estimate the time it takes clasts of varying sizes and vesicularities to reach the ocean surface from a depth of 900 m (Figure 6).

Consider a clast that is entirely filled with water vapor such that $f = 1$, where f is the fraction of pore space filled with water vapor. The clast has vesicularity, ϕ, initial temperature, T, diameter, D, and originates from a depth of 900 m. We assume an initial temperature of 850°C and calculate the initial density ρ_S, mass, m_s, and specific enthalpy, H, and total enthalpy, H_T, of internal the water vapor using a thermodynamic look-up table (IAPWS IF-97, XSteam;

Holmgren, 2006). We assume that the internal steam is fully coupled to the clast and cannot flow out unless the volume of steam exceeds the internal volume of the clast pore space. We calculate clast density as

$$\rho_c = \rho_r(1-\phi) + \rho_s\phi f + \rho_w\phi(1-f) \qquad \text{(B.1).}$$

where the subscripts *r* and *w* stand for rock and liquid water. Clast density changes primarily as a function of the volume of internal water vapor, which in turn is affected by cooling and decompression. Clasts lose thermal energy through cooling according to

$$\frac{dH_T}{dt} = -qFS \qquad (\mathrm{B.2}),$$

where q is an average rate of heat loss that was measured experimentally to be approximately 7.5 W cm^{-2} for initially air-filled pumice in water (Fauria, 2017), *S* is clast surface area, and *F* is a factor that describes the partitioning of latent heat within the water vapor and sensible heat within the glass. The ratio of sensible to latent heat in the clasts is characterized by the Stefan number

$$\mathrm{St} = \frac{\Delta T c_p}{\phi L} \sim 1 \qquad \text{(B.3),}$$

where ΔT, is the temperature difference between the initial clast temperature and ambient water, c_p is the heat capacity of the glass, and *L* is the latent heat of vaporization. We define

$$F = \frac{\phi L}{\Delta T c_p + \phi L} \qquad (\mathrm{B.4}).$$

The factor *F* accounts for sensible heat loss from the glass. That is, not all heat is drawn out of the internal water vapor, rather a proportion of cooling affects the glass. For an 850°C clast, we estimate $F \sim 0.5$. We find that precise value for *F* does not affect the calculated clast rise speeds, but is important for determining the minimum clast size that can reach the surface.

We calculate clast rise speeds as a function of clast density and size using equation (3). Clast rise distance Z through the water volume is

$$Z = \int U dt. \qquad (\mathrm{B}.5)$$

We relate depth h to pressure according to $P = \rho_w g h$. At each new depth we calculate the density and volume, V_s, of the internal water vapor as a function of pressure and specific enthalpy using a thermodynamic lookup table (XSteam; Holmgren, 2006). Internal water vapor can expand as clasts rise through the water column, and contract due to cooling. The volume fraction of pore space filled with water vapor is

$$f = \frac{V_s}{\phi V_c}. \quad (\mathrm{B}.6)$$

If the net effects of cooling, decompression, and gas expansion make the volume of internal water vapor exceed the volume of the pore space such that $f > 1$, we let all excess water vapor exit the pore space and set $f = 1$. We define the excess water vapor as $E_x = f - 1$. We write the change in water vapor mass and total enthalpy due to vapor escape from the clast as

$$\Delta m_i = -E_x V_c \phi \rho_{s,} \quad (\mathrm{B}.7)$$

$$\Delta H_T = -\Delta m_i H. \quad (\mathrm{B}.8)$$

In contrast, cooling can make contraction and condensation exceed decompression effects such that $f < 1$. If this is the case, we allow water liquid water to enter to pore space vacated by steam due to condensation (e.g., Fauria, 2017), but does not decrease the clast's enthalpy. Equation

(B.1) demonstrates, however, how ingested water increases clast density and thereby affects rise speed, decompression rates, and clast fate.

We solve equations (3) and (B.1-8) using a first order finite difference scheme. The model ends when a clast either reaches the ocean surface or becomes neutrally buoyant due to vapor condensation and water ingestion. Figure 4 shows how clast size affects rise time to the surface and the minimum clast sizes required to reach the surface from a depth of 900 m. Below these minimum clast sizes, cooling results in vapor condensation and buoyancy reversal before a clast can reach the surface (Figure 4).

Many of the assumptions in equations (B.2-B.8) and approximations needed to develop this model could, in principle, be relaxed with a full 3D multiphase flow model that includes gas exsolution from the melt and mass, momentum and energy exchange with the surrounding water, and the presence of unconnected porosity (Figure 4). The model used here also neglects the buoyant ascent of warm water that would entrain clasts. A model that couples clast-scale processes and large scale dynamics may improve the accuracy of calculations of the fate of clasts and may reveal new and neglected processes.

If there is unconnected porosity, and all the connected porosity fills with liquid water, the unconnected porosity is able to keep clasts floating if

$$\phi_u = \frac{(\rho_r - \rho_w)}{(\rho_w - \rho_s)}(1 - \phi_t) \quad (\mathrm{B.9})$$

where the subscripts on density are as before and *u* and *t* indicate unconnected and total porosity, respectively.

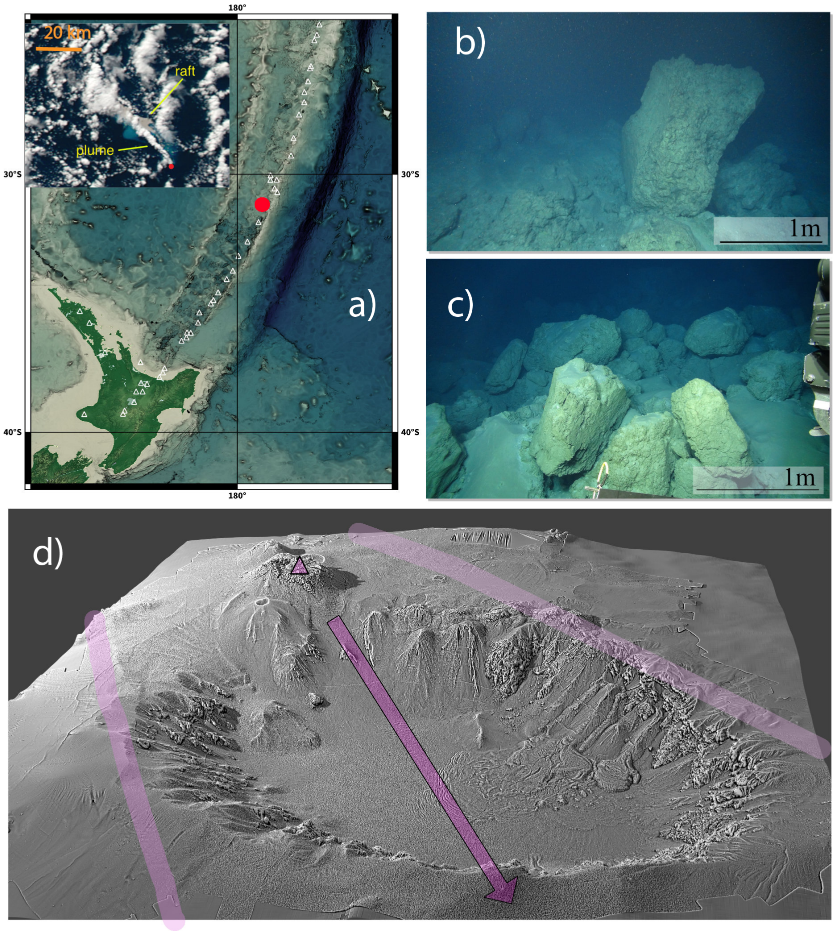

Figure 1: a) Location of the Havre volcano (red circle) in the Kermadec arc. Inset shows the raft and plume on 19 July, 01:26 UTC. Inset scale bar is 20 km long. Plume and raft show the transport direction to the northwest. Example seafloor giant pumice clasts showing curviplanar surfaces (b) and typical deposit (c). d) Shaded relief map showing the vent location (triangle) at a depth of 900 m; arrow shows the dispersal axis of seafloor giant pumice (the same as the transport direction in a), and the light purple lines bound the region containing those clasts. Caldera is 4.5 by 5 km in size. Viewing direction is looking south.

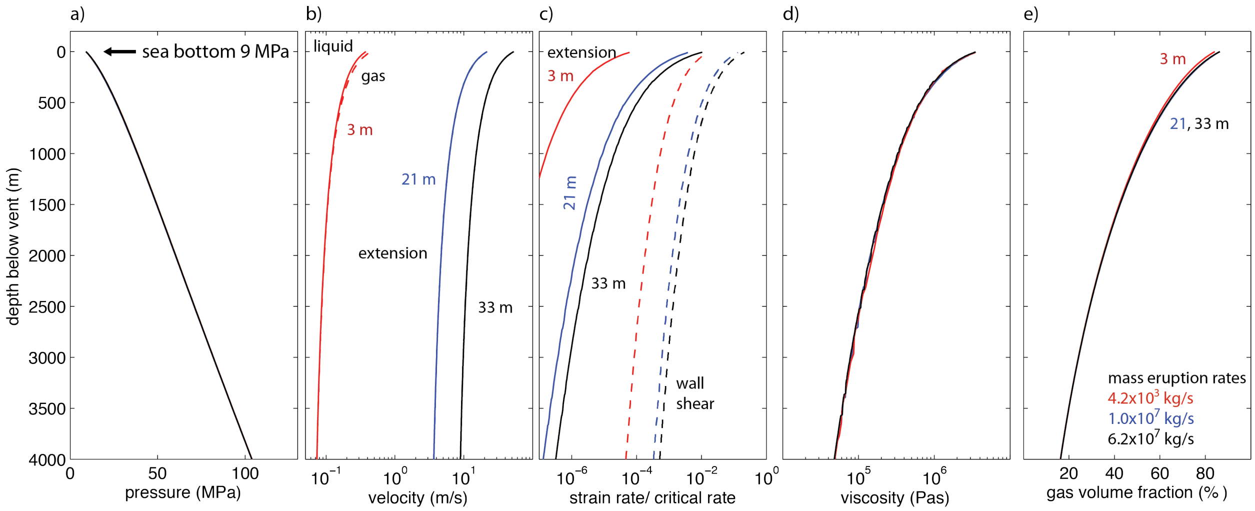

Figure 2: Magma ascent and gas escape, computed using the steady one-dimensional model of Degruyter et al. (2012) with melt properties for the Havre 2012 rhyolite eruption, showing how pressure (a), melt (solid curves) and gas (dashed curves) velocities (b), strain-rate relative to that needed to cause brittle fragmentation (c), magma viscosity (d), and vesicularity (e) varies with depth below the seafloor. Three conduit radii are assumed, 3, 21 and 33 m. Only the upper 4 km of the conduit are shown. Additional parameters: the percolation threshold for gas flow through the magma is zero, tortuosity factor is 3, bubble throat to radius ratio is 0.31, and the friction coefficient for gas flow through the magma is 10 (supplement S1 for details).

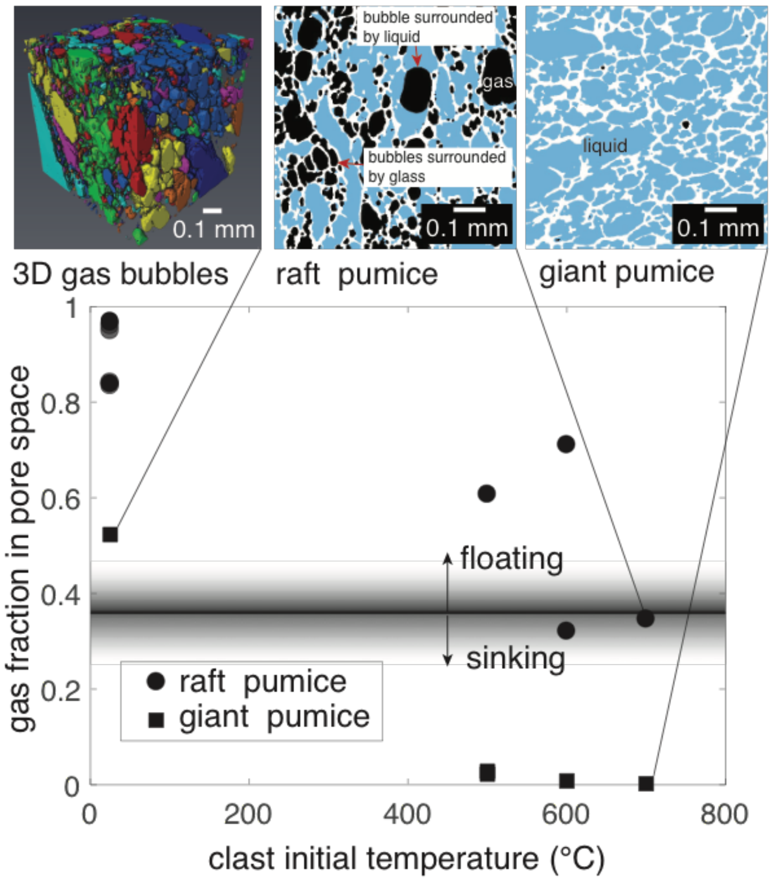

.

Figure 3: Initially hot pumice ingests more water than cold pumice, and giant pumice fragments (unknown locations within the larger clast) recovered from the seafloor ingest more water than pumice from the raft. A different pumice clast is used for each experiment and hence data point. The horizontal line shows the trapped gas fraction needed to keep a clast with a vesicularity of 80% buoyant. The two images on the upper right are 2D slices through their 3D images showing the distribution of glass (white), trapped gas (black), and liquid water (blue). Upper left shows the 3D shapes of trapped gas bubbles with a different color assigned to different gas bubbles.

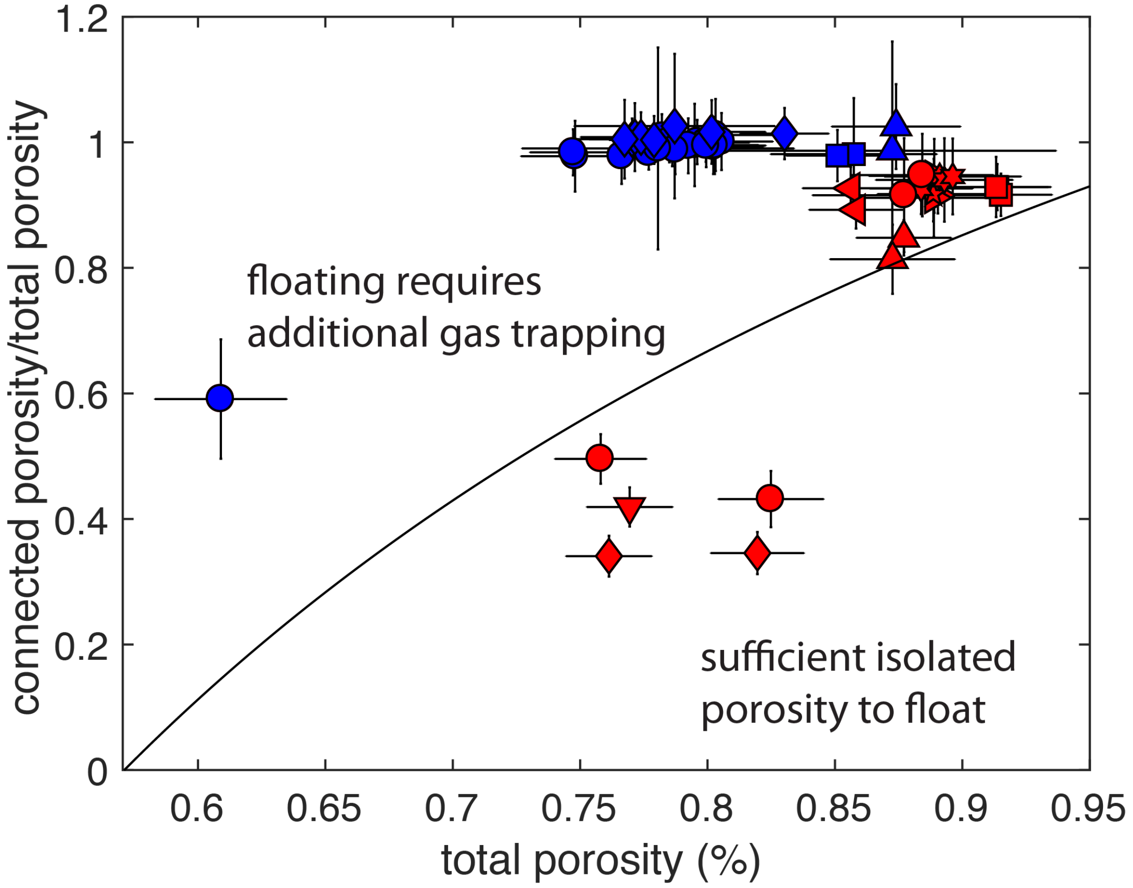

Figure 4: Connected fraction of total porosity vs. total porosity for seafloor giant pumice samples (red) and raft samples (blue). The measurements were conducted on multiple cores from three seafloor giant pumice samples and nine raft samples. Distinct samples are shown with different symbols. Excluding one seafloor measurement, which was collected from a breadcrusted exterior, the seafloor giant pumice samples all have > 99% connected porosity. All raft samples contain isolated vesicles. Shown with the curve is the amount of connected porosity needed, as a function of total porosity to allow clasts to sink if the connected pore space fills completely with water (equation B.9).

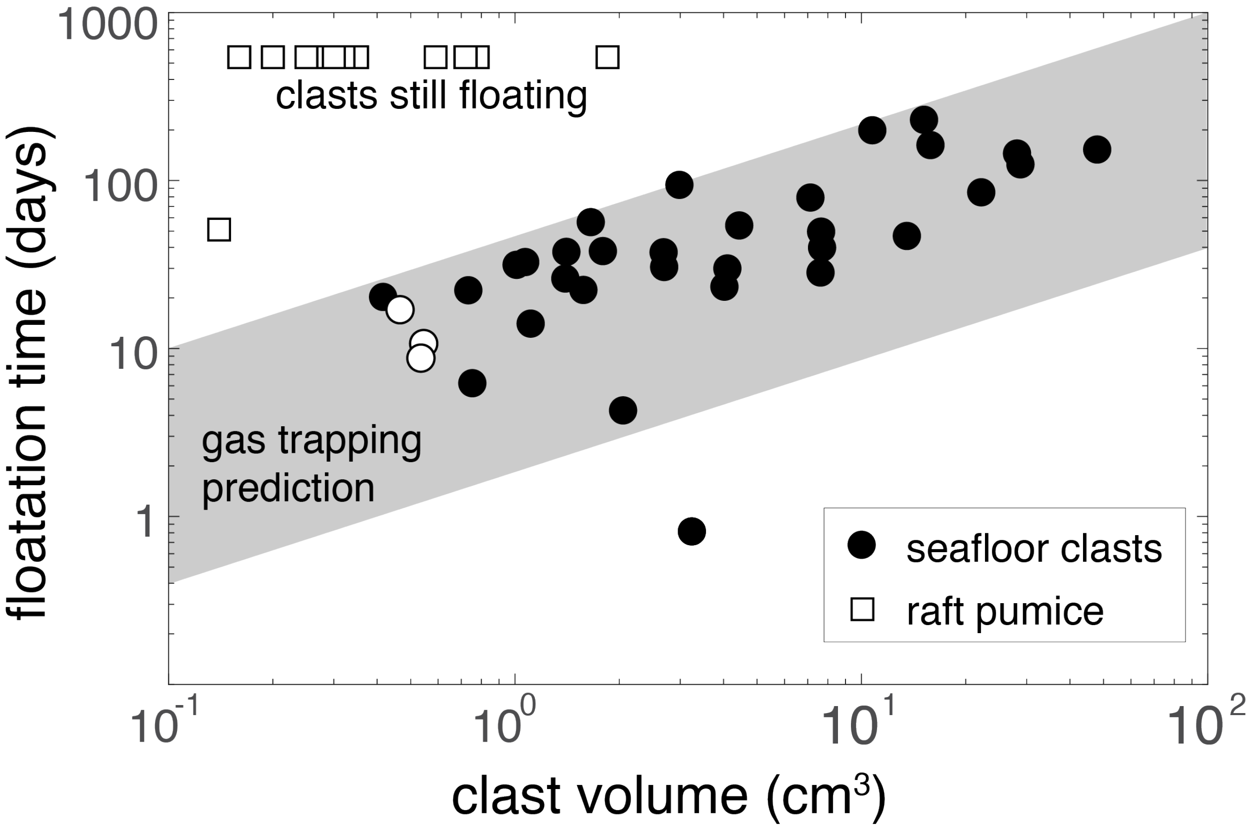

Figure 5: Clast volume versus floatation time (the time at which clasts sink). Data points above "still floating" show clasts that were still floating at the time of manuscript submission. Open data points represent clasts for which volume was calculated from weight and by assuming porosity; black data points represent clasts for which volume was measured using photogrammetry. From calculated porosity from mass and volume measurements we find that seafloor clasts have porosities of 85.6±3.2%. The grey bar represents a floatation time prediction from equation (2) and assuming $0.1 < \theta < 0.5$. The behavior of seafloor clasts matches the gas trapping prediction while that of raft clasts does not. Error bars are smaller than the data points.

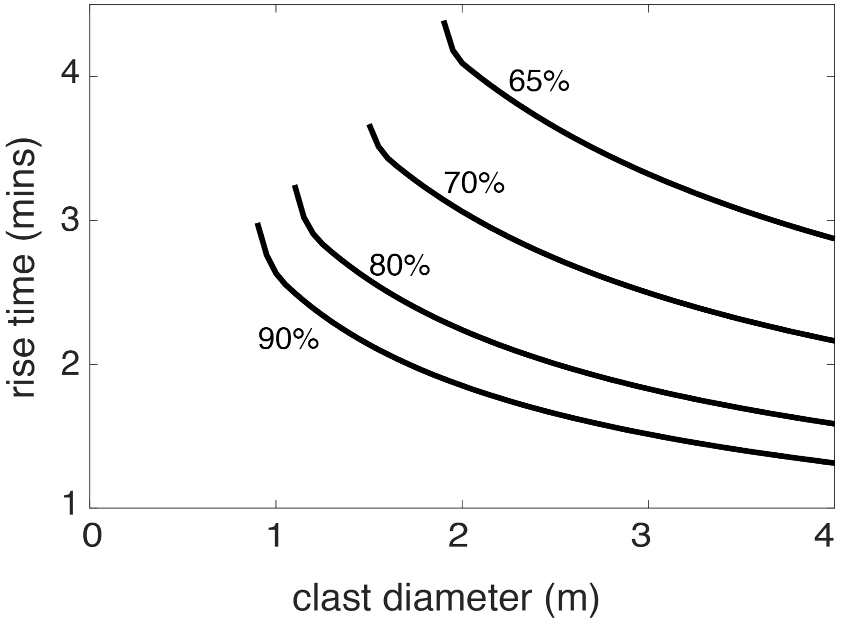

Figure 6: Time required for clasts to reach the ocean surface from a depth of 900 m as a function of their size and vesicularity (assumed constant during ascent). Clasts with diameters smaller than those for which the curves begin (to the left of the curves) will ingest enough water to become negatively buoyant before reaching the surface. Rise speed evolves according to equation (2) and clast density is computed from the water ingestion model (appendix B).

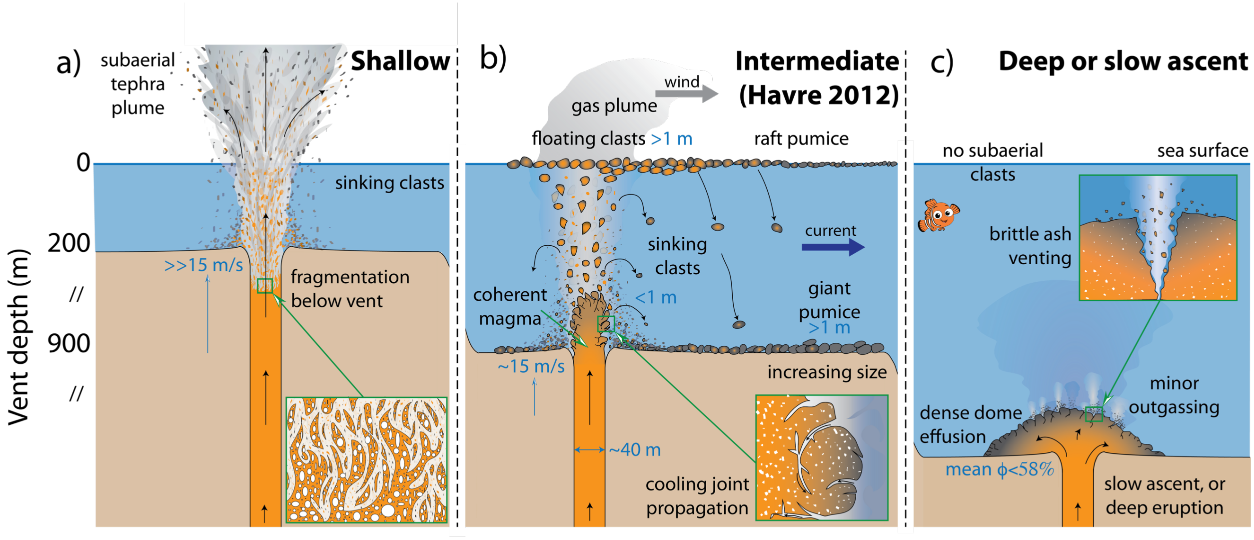

Figure 7: Schematic illustration of the eruption of magma with Havre composition and water content, but at different depths: a) shallow enough that fragmentation occurs in the conduit, b) Havre vent depth, and c) deep or ascended slow enough that vesicularity is < 58%. In b), clast size in the raft decreases with transport owing to abrasion. Inset in each panel illustrates the manner in which clasts might form, either within the conduit (a), or quenching in water (b and c). Panel b) illustrates the settling of smaller clasts close to the vent, the rise of large, hot clasts to the sea surface, the trapping of hot pumice beneath the sea surface, and the settling of giant pumice out of the raft due to water ingestion. The relative temperature gradient of melt to glass in clasts given from orange to grey, respectively. White shapes are vesicles. Liquid water is blue. Not to scale.

References cited

Allen, R. L., Weihed, P., & Svenson, S. A. (1996). Setting of Zn-Cu-Au-Ag massive sulfide deposits in the evolution and facies architecture of a 1.9 Ga marine volcanic arc, Skellefte District, Sweden. *Economic Geology*, *91*(6), 1022-1053.

Allen, S. R., Fiske, R. S., & Cashman, K. V. (2008). Quenching of steam-charged pumice: Implications for submarine pyroclastic volcanism. *Earth and Planetary Science Letters*, *274*(1), 40-49.

Allen, S. R., & McPhie, J. (2009). Products of neptunian eruptions. *Geology*, *37*(7), 639-642.

Allen, S. R., Fiske, R. S., & Tamura, Y. (2010). Effects of water depth on pumice formation in submarine domes at Sumisu, Izu-Bonin arc, western Pacific. *Geology*, *38*(5), 391-394.

Bagdassarov, N., & Dingwell, D. (1994). Thermal properties of vesicular rhyolite. *Journal of Volcanology and Geothermal Research*, *60*(2), 179-191.

Bredehoeft, J. D., & Papaopulos, I. S. (1965). Rates of vertical groundwater movement estimated from the Earth's thermal profile. *Water Resources Research*, *1*(2), 325-328.

Barker, S. J., Rotella, M. D., Wilson, C. J., Wright, I. C., & Wysoczanski, R. J. (2012). Contrasting pyroclast density spectra from subaerial and submarine silicic eruptions in the Kermadec arc: implications for eruption processes and dredge sampling. *Bulletin of volcanology*, *74*(6), 1425-1443.

Batchelor, G. K. (1967). An Introduction to Fluid Mechanics, 615 pp. *Cambridge University Press, New York*.

Burgisser, A., Chevalier, L., Gardner, J. E., & Castro, J. M. (2017). The percolation threshold and permeability evolution of ascending magmas. *Earth and Planetary Science Letters*, *470*, 37-47.

Carey, R. J., Wysoczanski, R., Wunderman, R., & Jutzeler, M. (2014). Discovery of the largest historic silicic submarine eruption. *Eos, Transactions American Geophysical Union*, *95*(19), 157-159.

Carey, R., Soule, S. A., Manga, M., White, J., McPhie, J., Wysoczanski, R., ... & Caratori-Tontini, F. (2018). The largest deep-ocean silicic volcanic eruption of the past century. *Science Advances*, *4*(1), e1701121.

Cas, R. A. F., & Wright, J. V. (1987). Volcanic Successions, Modern and Ancient: A Geological Approach to Processes, Products and Successions, 528 pp.

Cas, R. A., & Giordano, G. (2014). Submarine volcanism: a review of the constraints, processes and products, and relevance to the Cabo de Gata volcanic succession. *Italian Journal of Geosciences*, *133*(3), 362-377.

Cashman, K. V., & Fiske, R. S. (1991). Fallout of pyroclastic debris from submarine volcanic eruptions. *Science(Washington)*, *253*(5017), 275-280.

Colombier, M., Wadsworth, F. B., Gurioli, L., Scheu, B., Kueppers, U., Di Muro, A., & Dingwell, D. B. (2017). The evolution of pore connectivity in volcanic rocks. *Earth and Planetary Science Letters*, *462*, 99-109.

Costa, A. (2005). Viscosity of high crystal content melts: dependence on solid fraction. *Geophysical Research Letters*, *32*(22).

Degruyter, W., Bachmann, O., Burgisser, A., & Manga, M. (2012). The effects of outgassing on the transition between effusive and explosive silicic eruptions. *Earth and Planetary Science Letters*, *349*, 161-170.

Dufek, J., Manga, M., & Staedter, M. (2007). Littoral blasts: Pumice-water heat transfer and the conditions for steam explosions when pyroclastic flows enter the ocean. *Journal of Geophysical Research: Solid Earth*, *112*(B11).

Fauria, K. (2017) PhD dissertation, University of California, Berkeley.

Fauria, K. E., Manga, M., & Wei, Z. (2017). Trapped bubbles keep pumice afloat and gas diffusion makes pumice sink. *Earth and Planetary Science Letters*, *460*, 50-59.

Giachetti, T., Druitt, T. H., Burgisser, A., Arbaret, L., & Galven, C. (2010). Bubble nucleation, growth and coalescence during the 1997 Vulcanian explosions of Soufrière Hills Volcano, Montserrat. *Journal of Volcanology and Geothermal Research*, *193*(3), 215-231.

Giordano, D., Russell, J. K., & Dingwell, D. B. (2008). Viscosity of magmatic liquids: a model. *Earth and Planetary Science Letters*, *271*(1), 123-134.

Gonnermann, H. M., & Manga, M. (2005). Nonequilibrium magma degassing: results from modeling of the ca. 1340 AD eruption of Mono Craters, California. *Earth and Planetary Science Letters*, *238*(1), 1-16.

Gonnermann, H., Giachetti, T., Nguyen, C. T., Houghton, B. F., Crozier, J. A., & Carey, R. J (2017). Permeability during magma expansion and compaction. *Journal of Geophysical Research: Solid Earth*.

Holmgren, M. (2006). X Steam for Matlab. *www. x-eng. com, accessed November*, *20*, 2017.

Houghton, B.F., Hobden, B.J., Cashman, K.V., Wilson, C.J.N. and Smith, R.T. (2003). Large-Scale Interaction of Lake Water and Rhyolitic Magma During the 1.8 Ka Taupo Eruption, New Zealand. Explosive subaqueous volcanism, pp. 97-109.

Jutzeler, M., Marsh, R., Carey, R. J., White, J. D., Talling, P. J., & Karlstrom, L. (2014). On the fate of pumice rafts formed during the 2012 Havre submarine eruption. *Nature communications*, *5*.

Jutzeler, M., Manga, M., White, J. D. L., Talling, P. J., Proussevitch, A. A., Watt, S. F. L., Cassidy, R.N., Le Friant, A., & Ishizuka, O. (2017). Submarine deposits from pumiceous pyroclastic density currents traveling over water: An outstanding example from offshore Montserrat (IODP 340). *Geological Society of America Bulletin*, *129*(3-4), 392-414.

Kano, K. (2003). Subaqueous pumice eruptions and their products: A review. *Explosive subaqueous volcanism*, 213-229.

Kano, K., Yamamoto, T., & Ono, K. (1996). Subaqueous eruption and emplacement of the Shinjima Pumice, Shinjima (Moeshima) Island, Kagoshima Bay, SW Japan. *Journal of Volcanology and Geothermal Research*, *71*(2-4), 187-206.

Kato, Y. (1987). Woody pumice generated with submarine eruption. *Journal of the Geological Society of Japan, 93*, 11-20 (1987).

Kozono, T., & Koyaguchi, T. (2009). Effects of relative motion between gas and liquid on 1-dimensional steady flow in silicic volcanic conduits: 2. Origin of diversity of eruption styles. *Journal of Volcanology and Geothermal Research*, *180*(1), 37-49.

Kueppers, U., Nichols, A.R.L., Zanon, V., Potuzak, M., Pacheco, J.M.R., 2012. Lava balloons – peculiar products of basaltic submarine eruptions. Bull. Volcanol. 74, 1379–1393.

Llewellin, E. W., & Manga, M. (2005). Bubble suspension rheology and implications for conduit flow. *Journal of Volcanology and Geothermal Research*, *143*(1), 205-217.

Manville, V., White, J. D. L., Houghton, B. F., & Wilson, C. J. N. (1998). The saturation behaviour of pumice and some sedimentological implications. *Sedimentary Geology*, *119*(1), 5-16.

McPhie, J., & Allen, R. L. (2003). Submarine, Silicic, Syn-Eruptive Pyroclastic Units in the Mount Read Volcanics, Western Tasmania: Influence of Vent Setting and Proximity on Lithofacies Characteristics. *Explosive Subaqueous Volcanism*, 245-258.

Mitchell, S. J., McIntosh, I. M., Houghton, B. F., Carey, R. J., & Shea, T., (in review). Dynamics of a powerful deep submarine eruption recorded in H2O contents and speciation in rhyolitic glass: The 2012 Havre eruption, *Earth and Planetary Science Letters*

Mueller, S., Melnik, O., Spieler, O., Scheu, B., & Dingwell, D. B. (2005). Permeability and degassing of dome lavas undergoing rapid decompression: an experimental determination. *Bulletin of Volcanology*, *67*(6), 526-538.

National Academies of Sciences, Engineering and Medicine (2017). Volcanic eruptions and their repose, unrest, precursors, and time. Washington, DC: The National Academies Press. https://doi.org/10.17226/24650.

Olson, P., & Singer, H. (1985). Creeping plumes. *Journal of Fluid Mechanics*, *158*, 511-531.

Papale, P. (1999). Strain-induced magma fragmentation in explosive eruptions. *Nature*, *397*(6718), 425-428.

Putirka, K. D. (2008). Thermometers and barometers for volcanic systems. *Reviews in Mineralogy and Geochemistry*, *69*(1), 61-120.

Randolph-Flagg, N., Breen, S., Hernandez, A., Manga, M., & Self, S. (2017). Evenly spaced columns in the Bishop Tuff (California, USA) as relicts of hydrothermal cooling. *Geology*, *45*(11), 1015-1018.

Reynolds, M. A., Best, J. G., & Johnson, R. W. (1980). *1953-57 Eruption of Tuluman Volcano: Rhyolitic Volcanic Activity in the Northern Bismarck Sea* (Vol. 7). Geological Survey of Papua New Guinea.

Risso, C., Scasso, R. A., & Aparicio, A. (2002). Presence of large pumice blocks on Tierra del Fuego and South Shetland Islands shorelines, from 1962 South Sandwich Islands eruption. *Marine Geology*, *186*(3), 413-422.

Rotella, M. D., Wilson, C. J., Barker, S. J., & Wright, I. C. (2013). Highly vesicular pumice generated by buoyant detachment of magma in subaqueous volcanism. *Nature Geoscience*, *6*(2), 129.

Rotella, M. D., Wilson, C. J., Barker, S. J., Schipper, C. I., Wright, I. C., & Wysoczanski, R. J. (2015). Dynamics of deep submarine silicic explosive eruptions in the Kermadec arc, as reflected in pumice vesicularity textures. *Journal of Volcanology and Geothermal Research*, *301*, 314-332.

Rust, A. C., & Cashman, K. V. (2004). Permeability of vesicular silicic magma: inertial and hysteresis effects. *Earth and Planetary Science Letters*, *228*(1), 93-107.

Shea, T., Hammer, J., & First, E. (2013). Magma balloons or bombs? *Nature Geoscience*, *6*(10), 802-803.

Simmons, J. H. (1998). What is so exciting about non-linear viscous flow in glass, molecular dynamics simulations of brittle fracture and semiconductor–glass quantum composites. *Journal of non-crystalline solids*, *239*(1), 1-15.

Vella, D., & Huppert, H. E. (2007). The waterlogging of floating objects. *Journal of Fluid Mechanics*, *585*, 245-254.

van Otterloo, J., Cas, R. A., & Scutter, C. R. (2015). The fracture behaviour of volcanic glass and relevance to quench fragmentation during formation of hyaloclastite and phreatomagmatism. *Earth-Science Reviews*, *151*, 79-116.

von Lichtan, I. J., White, J. D. L., Manville, V., & Ohneiser, C. (2016). Giant rafted pumice blocks from the most recent eruption of Taupo volcano, New Zealand: Insights from palaeomagnetic and textural data. *Journal of Volcanology and Geothermal Research*, *318*, 73-88.

White, J.D., Schipper, C.I. and Kano, K. (2015). Submarine explosive eruptions. In *The Encyclopedia of Volcanoes (Second Edition)* (pp. 553-569).

Whitham, A. G., & Sparks, R. S. J. (1986). Pumice. *Bulletin of Volcanology*, *48*(4), 209-223.

Wilson, C. J. N., & Walker, G. P. (1985). The Taupo eruption, New Zealand I. General aspects. *Philosophical Transactions of the Royal Society of London A: Mathematical, Physical and Engineering Sciences*, *314*(1529), 199-228.

Wright, H., Roberts, J.J., Cashman, K.V., 2006. Permeability of anisotropic tube pumice: model calculations and measurements. Geophys. Res. Lett. 33 (17).

S1 Conduit model parameters

Magma ascent is modeled assuming steady isothermal two-phase flow in a cylindrical conduit with constant radius. The flow is one-dimensional with all properties varying only with depth. The equations solved are identical to those in Degruyter et al. (2012) with fragmentation criterion given by (1) and a few modifications. We fit a model for melt viscosity with the same functional form as that in Hess and Dingwell (1996) with viscosity computed from Giordano et al. (2008) and measured composition (S3),

$$\log\mu = -3.62517 + 0.248398\ln(100c) + \frac{9601 - 2368\ln(100c)}{T - (195.7 + 96.4931\ln(100c)}$$

where c is the water concentration in mass fraction and T is temperature.

The magma viscosity μ_m is given by

$$\mu_m = \mu(c, T)\theta(\chi)v(\phi)$$

where $\theta(\chi)$ accounts for the effects of crystals (5% assumed) on magma viscosity (Costa, 2005), and

$$v(\phi) = (1-\phi)^{5/3}$$

accounts for the effects of bubbles (Llewellin and Manga, 2005).

Other parameters used in the model include a gas viscosity of 10^{-5} Pa s, a conduit length of 8100 m, magma temperature of 850 ^{o}C, melt density of 2400 kg m^{-3}, initial water content of 5.8 weight %, initial pressure of 200 MPa, vent pressure of 9 MPa, bubble number density of 10^{14} m^{-3}, tortuosity factor m of 3, friction factor f_0 of 10, a throat/bubble size ratio f_{tb} of 0.3125, and a percolation threshold of 0 (continuous percolation).

References for S1

Costa, A. (2005). Viscosity of high crystal content melts: dependence on solid fraction. *Geophysical Research Letters*, *32*(22).

Degruyter, W., Bachmann, O., Burgisser, A., & Manga, M. (2012). The effects of outgassing on the transition between effusive and explosive silicic eruptions. *Earth and Planetary Science Letters*, *349*, 161-170.

Giordano, D., Russell, J. K., & Dingwell, D. B. (2008). Viscosity of magmatic liquids: a model. *Earth and Planetary Science Letters*, *271*(1), 123-134.

Hess, K. U., & Dingwell, D. D. (1996). Viscosities of hydrous leucogranitic melts: A non-Arrhenian model. *American Mineralogist*, *81*(9-10), 1297-1300.

Llewellin, E. W., & Manga, M. (2005). Bubble suspension rheology and implications for conduit flow. *Journal of Volcanology and Geothermal Research*, *143*(1), 205-217.

S2 Initial water content

Initial dissolved volatile contents *c* were measured using the CAMECA IMS 1280 secondary ion mass spectrometer at Woods Hole Oceanographic Institution, Massachusetts. H_2O, CO_2 and F contents were obtained from 16 plagioclase-hosted melt inclusions from a giant pumice block retrieved from the seafloor (Carey et al., in press). Melt inclusions analyzed ed had no visible fractures or pathways to the phenocryst edge and no vapor bubbles present.

Raw $^{16}O^{1}H/^{30}Si$ ratios from the SIMS were calibrated to H_2O wt % using calibration curves determined from a series of rhyolite standards and synthetic forsterite with known FTIR H_2O wt %. Likewise, CO_2 and F were determined using the raw $^{12}C/^{30}Si$ and $^{35}F/^{30}Si$ ratios from the samples and known CO_2 and F calibration curves from the standards. Measurements are summarized in Table S2.1.

H_2O and F contents were used in the initial melt viscosity calculation (supplement S1); F contents <0.1 wt % (1000 ppm) had a negligible effect on viscosity. Figure S2.1 shows that H_2O and CO_2 contents were also used to determine the initial model pressure of 200 MPa using the VolatileCalc solubility model (Newman and Lowenstern, 2002). H_2O-CO_2 isobars were determined for a rhyolitic melt at 850°C where all melt inclusions correspond to an average storage pressure of 200 MPa. The very low CO_2 contents (<150 ppm) justifies the use of only H_2O as the volatile phase within the conduit ascent model (S1).

Table S2.1 Measured volatile contents in melt inclusions of seafloor pumice clasts

SIMS data	**H_2O (wt %)**	**CO_2 (ppm)**	**F (ppm)**
Havre melt inclusions	5.74	22.8	963
	6.12	53.9	992
	5.66	124.3	955
	5.07	73.3	888
	6.85	8.8	970
	5.29	77.5	838
	5.83	58.6	996
	5.90	125.2	985
	5.83	33.0	966
	6.38	116.7	1040
	6.48	108.7	1054
	5.58	172.1	935
	5.61	127.9	931
	5.85	21.8	978
	5.81	36.5	901
	5.18	144.1	1022
Average	5.82	81.6	963

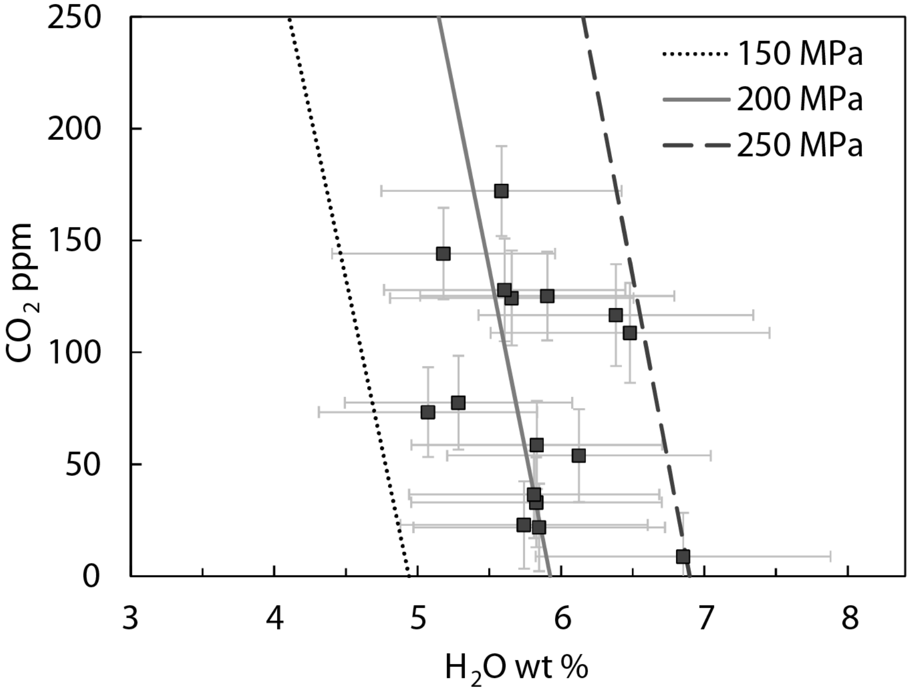

Figure S2.1 Measured CO_2 and H_2O in plagioclase-hosted melt inclusions with H_2O-CO_2 isobars were determined for a rhyolitic melt at 850°C.

References for S2

Newman, S., & Lowenstern, J. B. (2002). VolatileCalc: a silicate melt–H_2O–CO_2 solution model written in Visual Basic for Excel. *Computers & Geosciences*, *28*(5), 597-604.

S3 Melt composition

XRF data given in Table S3.1 are the average for 5 giant pumiceous blocks sampled from the seafloor. Values match very well with those from Carey et al. (in press) and Rotella et al., (2015). Fe_2O_3 is corrected to FeO_t for use in the viscosity model (supplement S1).

We assume the initial melt composition is the same as the whole rock plus dissolved water.

Table S3.1 Whole rock composition.

SiO_2	**TiO_2**	**Al_2O_3**	**FeO_t**	**MnO**	**MgO**	**CaO**	**Na_2O**	**K_2O**	**P_2O_5**	**Total**	**LOI**
72.437	0.479	14.145	3.017	0.122	0.727	2.608	5.117	1.590	0.083	100.325	1.131

S4 X-ray computed microtomography

X-ray microtomography was performed on beamline 8.3.2 at the Advanced Light Source, Lawrence Berkeley National Lab. We used 30 kev monochromatic x-rays, a 5X lens to obtain a voxel size of 1.22 microns, and used 1024 images and the TomoPy gridrec algorithm (Gursoy et al., 2014) to create the 3D images.

To segment the 3D images into water, gas and glass, we used the Fiji trainable Weka segmentation algorithm (Hall et al., 2009) by manually outlining gas, liquid and glass and retraining the classifiers until the segmentation seemed accurate. The volume fraction of each phase was computed from the binary segmented images in Fiji. Aviso was used to make the images in Figure 4 and to identify distinct bubbles in the 3D rendering.

References cited in S4

Gürsoy, D., De Carlo, F., Xiao, X., & Jacobsen, C. (2014). TomoPy: a framework for the analysis of synchrotron tomographic data. *Journal of synchrotron radiation*, *21*(5), 1188-1193.

Hall, M., Frank, E., Holmes, G., Pfahringer, B., Reutemann, P., & Witten, I. H. (2009). The WEKA data mining software: an update. *ACM SIGKDD explorations newsletter*, *11*(1), 10-18.

Supplement S5: Pumice floatation experiments

The seafloor clasts used here were fragments from decimeter pumiceous Havre seafloor samples HVR 020 and HVR 022 (Figure S5.1). We do not distinguish between HVR 020 and HVR 022 in our experiments because these two samples were mixed together when we retrieved them. The raft pumice was provided by Melissa Rotella from samples collected in New Zealand (Rotella et al., 2015), and the clasts we used were rounded by abrasion in the raft. These are different clasts than those used for the connected porosity measurements in Figure 4.

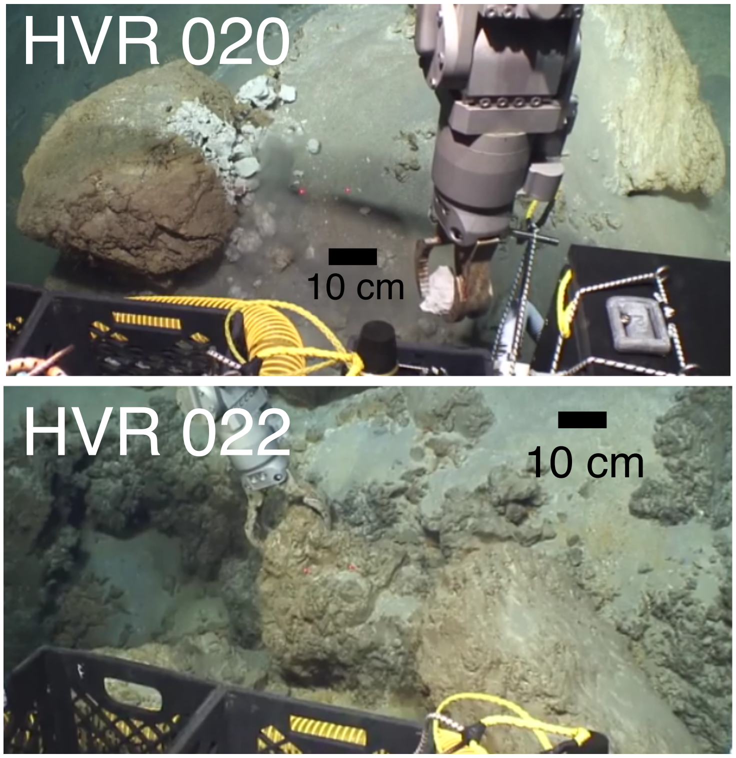

Figure S5.1: Havre seafloor clasts used in the pumice floatation experiments. HVR 020 and HVR 022 are both decimeter pumiceous clasts. The images show the clasts at the time of sample collection (Carey et al., in press).

Table S5.1 Experimental results and measurements of pumice floatation time. * refers to values that were calculated assuming a clast porosity of 83% and "nd" means not directly measured.

pumice name	type	weight (g)	volume (cm^3)	porosity	floatation time (days)
MDR_01	raft	0.058	*0.14	nd	51.03
MDR_02	raft	0.141	*0.35	nd	> 532
MDR_03	raft	0.132	*0.32	nd	> 532
MDR_04	raft	0.064	*0.16	nd	> 532
MDR_05	raft	0.116	*0.28	nd	> 532
MDR_06	raft	0.082	*0.20	nd	> 532
S1_07	raft	0.755	*1.85	nd	> 532
S1_08	raft	0.319	*0.78	nd	> 532
S1_09	raft	0.241	*0.59	nd	> 532
S1_10	raft	0.292	*0.72	nd	> 532
S1_11	raft	0.121	*0.30	nd	> 532
S1_12	raft	0.294	*0.72	nd	> 532
S1_13	raft	0.1	*0.25	nd	> 532
S1_14	raft	0.034	*0.08	nd	> 532
HVR 001	seafloor	1.646	4.14	0.83	29.4
HVR 002	seafloor	1.048	2.71	0.84	36.7
HVR 003	seafloor	0.71	2.07	0.86	4.2
HVR 004	seafloor	0.238	1.02	0.90	30.9
HVR 005	seafloor	0.646	1.67	0.84	55.5
HVR 006	seafloor	0.647	1.59	0.83	21.9
HVR 007	seafloor	0.177	0.42	0.82	19.9
HVR 008	seafloor	0.349	1.08	0.87	32.1
HVR 009	seafloor	0.567	1.41	0.83	25.6
HVR 010	seafloor	0.404	0.76	0.78	6.1

HVR 011	seafloor	0.446	1.42	0.87	36.9
HVR 012	seafloor	0.249	0.74	0.86	21.8
HVR 013	seafloor	0.423	1.12	0.84	13.8
HVR 015	seafloor	0.905	3.01	0.88	92.5
HVR 016	seafloor	0.228	0.54	0.83	8.6
HVR 017	seafloor	0.192	*0.47	nd	16.7
HVR 018	seafloor	1.747	3.27	0.78	0.8
HVR 018	seafloor	1.747	3.27	0.78	0.8
HVR 019	seafloor	0.539	1.81	0.88	37.3
HVR 020	seafloor	0.925	2.72	0.86	30
HVR 021	seafloor	5.465	15.97	0.86	159.5
HVR 022	seafloor	9.931	22.38	0.82	83.5
HVR 023	seafloor	14.601	29.04	0.79	122.5
HVR 024	seafloor	22.521	48.37	0.81	150.1
HVR 025	seafloor	0.224	*0.55	nd	10.5
HVR 026	seafloor	11.432	28.39	0.83	142.1
HVR 028	seafloor	6.632	13.65	0.80	45.9
HVR 030	seafloor	0.222	*0.54	nd	8.6
HVR 031	seafloor	5.481	15.30	0.85	225.6
HVR 032	seafloor	4.121	7.72	0.78	48.7
HVR 033	seafloor	1.461	4.06	0.85	22.9
HVR 034	seafloor	2.252	4.48	0.79	53
HVR 035	seafloor	2.817	7.19	0.84	77.7
HVR 036	seafloor	3.648	10.85	0.86	195.5
HVR 037	seafloor	3.69	7.77	0.80	39.1
HVR 038	seafloor	2.803	7.69	0.85	27.8